Implications of Multiple Corona Bursts in Lightning Processes for Radio Frequency Interferometer Observations

Ningyu Liu[1], Olaf Scholten[2], Joseph R. Dwyer[1], Brian M. Hare[2], Christopher F. Sterpka[1], Julia N. Tilles [3], and Frank D. Lind[4]

[1]Department of Physics and Astronomy & Space Science Center (EOS), University of New Hampshire, Durham, New Hampshire, USA
[2]University Groningen, Kapteyn Astronomical Institute, Landleven 12, 9747 AD Groningen, The Netherlands
[3]Sandia National Laboratories, Albuquerque, NM, USA
[4]MIT Haystack Observatory, Westford, Massachusetts, USA

Key Points:

- Complications of lightning radio interferometer data interpretation due to random nature of the emission sources are investigated
- Multiple corona bursts observed by LOFAR in lightning may be seen as a fast ($> 10^7$ m/s) moving source by typical lightning interferometers
- The resolution of typical lightning interferometers needs to be improved to resolve the structure in lightning processes

Corresponding author: Ningyu Liu, Ningyu.Liu@unh.edu

Abstract

Recent observations from LOFAR indicate that multiple, spatially distributed corona bursts can occur in lightning processes on the order of 10 microseconds. The close proximity of the corona bursts in space and time poses a great observation challenge for dedicated lightning radio interferometers, typically with <100 m baselines. This paper reports simulations to show the interferometry results that would be obtained with a typical lightning interferometer for such a lightning process. In particular, spatially-separated corona bursts at fixed locations may be seen as a fast ($> 10^7$ m/s) propagating source for an instrument with resolution greater than the spatial separation of the bursts. The implications and suggestions for lightning interferometry studies are discussed in the paper.

Plain Language Summary

Lightning evolution contains brief processes that are critical to its channel formation, but their physical mechanisms are poorly understood at present. Those processes emit very high frequency radio emissions, and radio sensor arrays have been used to detect those emissions to investigate their source processes. The latest observations from the large radio telescope LOFAR show that multiple, intense bursts of radio emission at discrete locations occur in those processes. Here we report simulations to show that such bursts are seen as a fast propagating wave for a typical lightning radio sensor array. Our study suggests that caution is required when interpreting the observations made with such a radio sensor array.

1 Introduction

Lightning is a complex and multiscale electrical phenomenon that generates a broad spectrum of electromagnetic radiation. Fast electrical discharge processes occur during lightning development and they generate high frequency (HF, 0.3-3 MHz) and very high frequency (VHF, 30-300 MHz) electromagnetic emissions. These radio frequency (RF) emissions have been utilized to map and/or image lightning via some form of interferometry analysis. Important advances have recently been made based on broadband HF/VHF interferometer observations. These include identification of fast breakdown processes capable of initiating lightning (Rison et al., 2016; Stock et al., 2017; Tilles et al., 2019; Huang et al., 2021), measurement of perpendicular-to-channel polarization of the radiation of dart leaders (Shao et al., 2018), discovery of needle-like structures on positive leaders (Hare et al., 2019; Pu & Cummer, 2019), and observation of corona bursts of negative leaders at high altitudes (Scholten et al., 2021a). Because the lightning VHF sources can have complex temporal, spatial, and spectral properties, the radiation amplitude has a very large dynamic range, and they occur in a generally noisy environment, lightning interferometer observation and interpretation is definitely not a trivial task.

Modeling and theoretical work has shown that filamentary streamer discharges can radiate strongly in the HF and VHF bands (Shi et al., 2016, 2019), and they are believed to be the main source of the HF and VHF radiation from lightning (Liu et al., 2019, 2020; Liu & Dwyer, 2020). For many lightning processes, such as a leader step or lightning initiating fast breakdown, a large number (10^5-10^8) of streamers are believed to be involved (Liu et al., 2019, 2020; Liu & Dwyer, 2020). Those processes have a typical timescale of at least one microsecond and a spatial scale of at least a few meters, in contrast to the nanosecond timescale and centimeter spatial scale of a streamer. The large difference in those scales implies that there is inherent random nature in both spatial and temporal distributions of streamer occurrences in a lightning process.

In this study, we attempt to demonstrate how the random nature of streamer occurrences in a lightning process can complicate the analysis of lightning interferometer observations. Our study focuses on the initiation stage of lightning, which typically contains only few channel branches, making the analysis of the interferometer observation easier. One common feature in the RF observation of lightning initiation is that a train of strong bipolar pulses occurs in the first few milliseconds (e.g., Nag et al., 2009; Marshall et al., 2014; Belz et al., 2020; Tilles, 2020). They are called initial breakdown pulses (IBPs), which are best observed by a RF sensor sensitive to lower RF frequency bands (e.g., 1 kHz-1 MHz). The duration of an IBP varies from 20 to 100 μs, with a mean of $\sim$60 μs. There are usually narrow subpulses superimposed on the initial half cycle of the waveform (e.g., Nag et al., 2009; Belz et al., 2020; Tilles, 2020).

A typical broadband VHF interferometer for lightning observation consists of three radio sensors with a baseline shorter than 100 m (Sun et al., 2013; Stock et al., 2014; Rison et al., 2016; Stock et al., 2017; Shao et al., 2018; Lyu et al., 2019; Tilles et al., 2019, 2020; Belz et al., 2020). The passband of the sensor spans from the upper HF band to the lower VHF band, e.g., 10-90 MHz for the interferometer developed by the New Mexico Tech (Stock et al., 2014; Rison et al., 2016). The resulting angular resolution limit for non super-resolution analysis is $\lambda/b = 0.06$ radians, where λ is the wavelength and b is the baseline length, corresponding to 600 m at a distance of 10 km. The observations obtained with such an interferometer indicate that IBPs are coincident with strong VHF bursts and the VHF source activity shows greatly accelerated vertical motion over a distance of 100 m or so, typically during the initial half cycle of the IBP. The speed of the accelerated vertical motion exceeds 10^7 m/s (Belz et al., 2020; Tilles, 2020). It has been proposed that IBPs are generated by fast breakdown, the same as narrow bipolar events (NBEs) (Belz et al., 2020). Belz et al. (2020) also found that gamma-ray production by lightning is directly connected to strong IBPs.

Better resolution can be achieved with a large radio telescope like LOFAR (Hare et al., 2019, 2020; Scholten et al., 2021a, 2021b). A recently-developed interferometry imaging code called interferometric 3-Dimensional (TRI-D) imager allows for meter scale accuracy in the LOFAR emission sources at a temporal resolution of 100 ns, which is able to show the structures within a lightning leader step (Scholten et al., 2021b) (see (Hare et al., 2020) as well for the leader step structure). The results reported by Scholten et al. (2021) indicate that during an IBP multiple corona bursts occur at discrete locations within a volume of approximately $100 \times 100 \times 100$ m^3 and there is no indication of a continuously propagating wave of intense electrical breakdown.

In this paper, we present simulations to show the results a typical lightning interferometer with a small number of elements would obtain for IBPs consisting of multiple corona bursts and to give some ideas on the requirements for an interferometer to resolve those corona bursts.

2 Simulation Model

The main goal of simulation is to reproduce the interferometer images of synthetic VHF sources with specified spatial and temporal properties to understand the interferometer observations. The simulation consists of two main stages. The first stage simulates the VHF radiation from sources and the signals recorded by the sensors. At the second stage, the signals are processed and then used to obtain the image of the source with interferometry analysis.

Figure 1a shows a plan view of the observation geometry considered in our simulation. For simplicity, we consider an interferometer of three elements only. The sensors form an equilateral triangle as shown by the three closely-packed triangles in the figure, with one of the baselines parallel to the x axis. The VHF emission sources are at $x =$

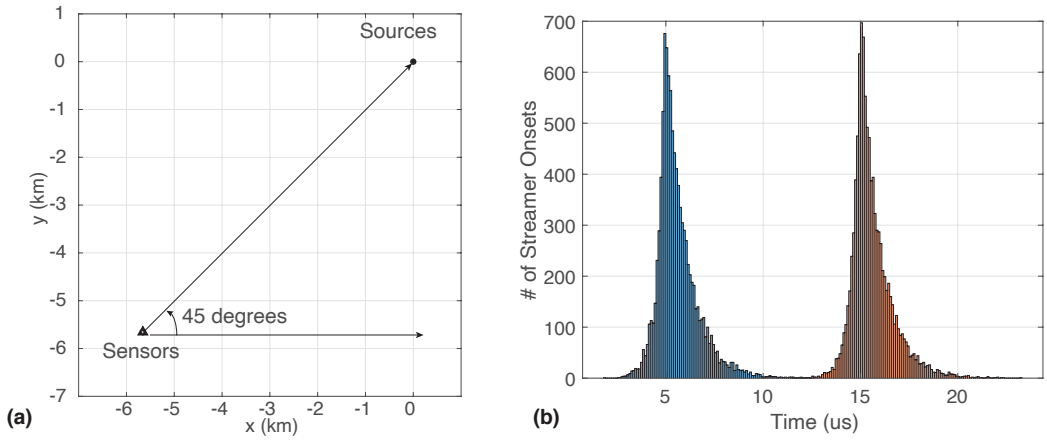

Figure 1. (a) Observation geometry in the simulation. (b) Histogram of the streamer onset.

$y = 0$, and the plan distance from the center of the sensor triangle to the source is 8 km, i.e., the center of the sensor triangle is at (8 km, -135°) in polar coordinates. The sources are at approximately 6 km altitude, and the distance from a sensor to the source is then about 10 km. This geometry closely represents the IBPs in cloud-to-ground lightning analyzed in (Tilles, 2020).

In the simulation, the right most sensor is set as the reference sensor or viewing point, for which the interferometric images are constructed. Its location varies as the baseline changes, because the location of the sensor triangle center is fixed. The images are made for a small area of 1.6° azimuth and 2° elevation centered around the centroid of the sources. In this setting, the location of the center of the image relative to the reference antenna varies when the baseline length changes, and its azimuth is about 45°, but not exactly.

2.1 Simple Model for VHF Radiating Corona Bursts in IBPs

The VHF radiation source model used in our study is formulated based on LOFAR observations. As mentioned in Introduction, the LOFAR data indicate that an IBP contains multiple corona bursts at different locations. In our simulation, we simply assume there are two corona bursts at two different altitudes: 6.1 km and 6.0 km, i.e., a 100 m height difference. We further assume that each burst contains 10^4 streamers, with the burst at the higher altitude occurring a few microseconds earlier. The onset times of the streamers within a burst are randomly drawn from an asymmetric Laplace distribution, with a 0.4 μs rise time and 1 μs fall time. Figure 1b shows the histogram of the streamer onset for a simulation case reported below, where the peaks of the two bursts are separated by 10 μs in time.

The streamers are assumed to be identical, and each generates a brief current pulse, which is assumed to be a double exponential function with a rise time of 1 ns and a fall time of 250 ns (Liu et al., 2019; Liu & Dwyer, 2020). The streamer current pulse and spectrum of the radiated field are shown by Figure S1 in Supplementary information.

2.2 Cross-correlation Based Imaging Technique

To construct the image using the recorded signals, we adopt the same cross-correlation based imaging technique as Stock (2014) and Tilles et al. (2019). Cross-correlations between signals from pairs of sensors are calculated and used to assign intensities to im-

age pixels. In addition, a beamforming technique is implemented in our simulation in order to improve the temporal resolution and accuracy. If we know where the source region is, we can use the center of the source region to estimate the respective time delays from the source to the sensors and then use the estimated delays to preliminarily align the signals. In this way, a smaller time window can be used to calculate the cross-correlation, which improves the temporal resolution.

The above description can be represented mathematically as follows. Suppose the time series recorded by each sensor is denoted by $E_i(t)$ and the time-shifted signal by $E_i^{\mathrm{o}}(t)$, we have

$$E_i^{\mathrm{o}}(t) = E_i(t + \tau_i), \tag{1}$$

where τ_i is the light travel time from the center of the source region to the ith sensor. The center of the source region is also set as the center (denoted by point o) of the image in the simulation. Let d_i^{o} represent the distance between point o and the ith sensor, then $\tau_i = d_i^{\mathrm{o}}/c$.

To obtain the beamformed image frame corresponding to a time interval $[t_n, t_n + T]$, where T is the time integration window size or exposure time of the image, the cross correlation between every pair of antennas i and j, R_{ij}^{o}, is calculated:

$$R_{ij}^{\mathrm{o}}(t_n, \tau_{ij}) = \int_{t_n}^{t_n+T} E_j^{\mathrm{o}}(t + \tau_{ij}) E_i^{\mathrm{o}}(t) dt, \tag{2}$$

where τ_{ij} is the time delay between the time-shifted series. Substituting equation (1) into (2) and changing the integration variable to $(t + \tau_i)$,

$$R_{ij}^{\mathrm{o}}(t_n, \tau_{ij}) = \int_{t_n+\tau_i}^{t_n+\tau_i+T} E_j(t + \tau_{ij} + \tau_j - \tau_i) E_i(t) dt = R_{ij}(t_n + \tau_i, \tau_{ij} + \tau_j - \tau_i). \tag{3}$$

Note $R_{ij}(t_n + \tau_i, \tau_{ij} + \tau_j - \tau_i)$ is the cross correlation between the non-shifted time series. From the observation geometry, we have $(d_{ij} \cos \alpha_{ij})/c = \tau_{ij} + \tau_j - \tau_i$, where d_{ij} is the baseline and α_{ij} is the directional angle. So

$$\tau_{ij} = \frac{d_{ij} \cos \alpha_{ij}}{c} - \tau_j + \tau_i. \tag{4}$$

Equation (4) relates the directional angle to the delay between the shifted time series of the two sensors.

For each pixel, its directional angle with respect to a baseline is calculated first and the corresponding delay τ_{ij} between the two shifted time series is found by using equation (4). The intensity of the pixel is then given by $R_{ij}^{\mathrm{o}}(t_n, \tau_{ij})$. For the last step, interpolation is necessary as $R_{ij}^{\mathrm{o}}(t_n, \tau_{ij})$ is found at discrete times or only the cross correlations at discrete angels α_{ij} are known. Test runs indicate a higher order interpolation scheme is necessary to obtain accurate results, and cubic spline interpolation with the not-a-knot end condition is used in our study. Furthermore, the same interpolation scheme is also used to preliminarily align the signals at the beamforming step.

Intensities from all baselines are then added together to obtain the total intensity of that pixel. Denote the intensity of the nth frame from a baseline as $I_{ij}(n, \alpha_{ij}) = R_{ij}^{\mathrm{o}}(t_n, \tau_{ij})$, we have

$$I(n, \vec{r}) = \sum_{i}^{M} \sum_{j=i+1}^{M} I_{ij}(n, \alpha_{ij}), \tag{5}$$

where M is the total number of sensors.

If the ith antenna is the reference antenna, the time of the nth image frame is set to $(t_n + T/2 + \tau_i)$.

Table 1. Parameters of the Four Simulation Cases

Case	Burst Time Separation (μs)	Passband (MHz)	Baseline (m)	Integration Time Window (μs)	Frame Time Shift (μs)
A	10	10-90	100	1.4	0.35
B	10	30-80	100	0.1	0.1
C	5	30-80	800	0.1	0.1
D	10	100-200	200	0.02	0.02

3 Results

Results from four simulation cases are presented below, and Table 1 gives the parameters of each simulation case. We consider two values for the time separation between the two bursts: 5 and 10 μs. Given the duration of IBPs, 10 μs represents a moderate value of the time separation between the bursts, and 5 μs for relatively narrow IBP pulses. In calculating the radiated electric field, a time step of 1 nanosecond (i.e., 1 GHz sampling frequency) is used. For each case, a bandpass filter is applied to the recored signals to obtain the specified bandwidth. Frame time shift is the time between two consecutive images, and there is no sample overlap between the images except for Case A, where the time shift is one quarter of the time integration window. Case A represents the typical configuration that was used in (Tilles et al., 2019, 2020; Tilles, 2020). As a large time integration window is used for this case, it is unnecessary to apply the beamforming technique. Except the baseline and the number of antennas, Cases B and C represent the configuration of the latest LOFAR studies (Scholten et al., 2021b, 2021). The last case is a system that represents a moderate increase in both the passband frequency and baseline of a typical radio interferometer dedicated to lightning research.

Figure 2 presents the simulation results from Case A. The three images correspond to three different time intervals, with their respective center times given in the figure. The bandwidth limited signal in Figure 2b shows although the two bursts are nominally separated by 10 μs, streamer activity is nearly continuous between them. The circles in Figure 2c give the heights (relative to 6 km) of the maximum intensity pixel of the images, while Figure 2d shows the temporal variation of the intensity of the same pixel. Each image in Figure 2a corresponds to either a peak or trough in Figure 2d. The large size of the main lobe in each image even under a narrow display intensity range is consistent with the nominal angular resolution of this case: $\lambda/b \simeq 0.06$ radians or 3.4 degrees. Before 44 μs or slightly after 46 μs, the maximum intensity pixel overlaps with the location of the active streamer burst. The smooth transition in height from approximately 80 m to 20 m, starting slightly after 44 μs and ending slightly after 46 μs, makes it appear that the source moves with a speed of $\simeq 3\times10^7$ m/s. The image at 45.753 μs shows that the maximum intensity pixel of that image is approximately at the mid point between the two bursts. Figure 2d shows that the intensity reaches the maximal value at the peaks of the bursts and is relatively small between the two bursts. The difference between the maximal and minimal values is, however, less than three orders of magnitude (note that the maximal intensity shown in the image at 45.753 μs is less than three orders of magnitude than the other two images), which is well within the dynamic range of a RF sensor of at least 12 bits. The image is made for a constant radial distance from the reference center, equal to the distance from the reference sensor to the center of the image at the mid point between the two bursts, i.e., (0 m, 0 m, 6050 m). This causes the heights of the two bursts are not exactly at 0 and 100 m (i.e., 6 and 6.1 km relative to ground), respectively.

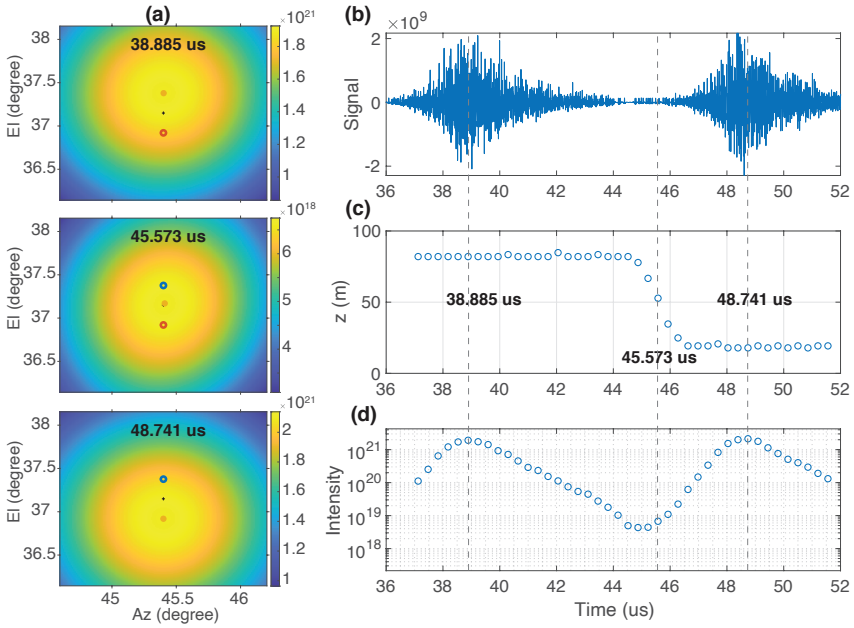

Figure 2. Case A simulation results. (a) Images at three different times. In each image, black '+' represents the center of the image, the two circles give the locations of the two streamer bursts, and the solid circle shows the location of the maximum intensity pixel. (b) The bandwidth limited signal from the reference sensor. (c) The height of the maximum intensity pixel relative to 6 km altitude. (d) The value of the maximum intensity pixel.

Figure 3 shows the simulation results from Case B. As the baseline is the same between this case and Case A and the frequency passband is approximately the same, the images of Case B are similar to those shown in Figure 2, which are omitted here. The apparent fast descending motion of the source can also be seen around 44-46 μs, with a similar change in the height and thus a similar speed. Because the time integration window is more than a factor of ten smaller than Case A, the fluctuations in the height and intensity of the maximum intensity pixel are much larger. The smaller time integration window also results in smaller intensity values.

Figure 4 presents the results from cases C and D. For Case C, the baseline is increased to 800 m while the bandwidth is kept the same as Case B, resulting in a much better angular resolution. The main lobe in Figure 4a is much smaller in size, comparing to those in Figure 2a. Figure 4b shows that the streamer activity continuously occurs from the beginning of the first burst through the end of the second burst. It is clear, however, from Figure 4c that the sources have discrete locations instead of forming a gradual descending trajectory. Due to the random nature of the streamer onset in each burst, the locations of the maximum intensity pixel between the two bursts can jump between the two true source locations. Finally, because of the smaller time separation between the bursts, the minimum intensity is less than two orders of magnitude smaller than the maximum intensity, as shown by Figure 4d. Overall, the increased baseline or improved angular resolution allows for resolving the two bursts even with a smaller time separation of 5 μs.

For Case D, both the passband frequency and baseline are moderately increased from Case A, so the angular resolution is better than Case A. The size of the main lobe shown in Figure 4e is smaller than that of Case A, but not as small as that of Case C. The time integration window 20 ns of this case is twice the reciprocal of the bandwidth,

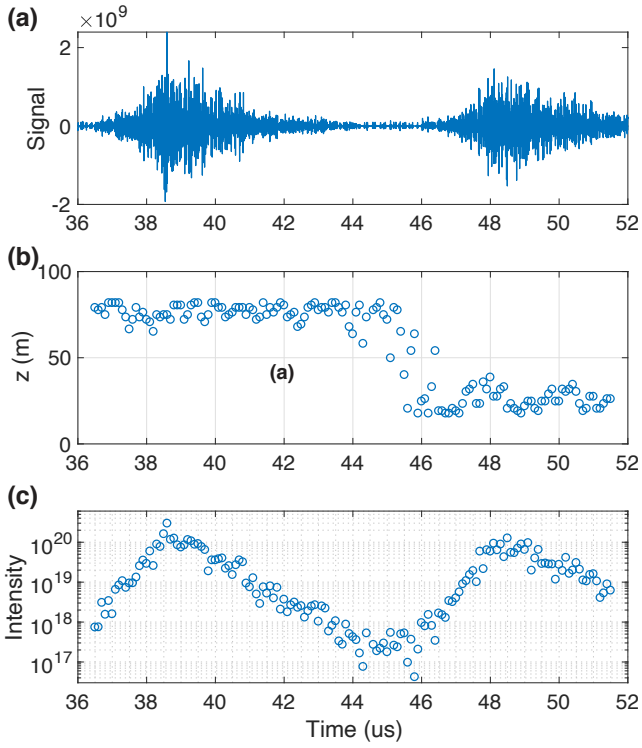

Figure 3. Case B simulation results. (a) The bandwidth limited signal from the reference sensor. (b) The height of the maximum intensity pixel relative to 6 km altitude. (c) The value of the maximum intensity pixel.

and beamforming is definitely required in order to use such a small time window. For this configuration, simply tracking the location of the maximum intensity pixel can tell that the radiation is not produced by a single moving source but by sources at discrete locations. Abrupt changes in the source height do occur in the time interval between the two bursts. The source height there is determined by which burst happens to generate stronger radiation in the corresponding 20 ns time window. Consistently, sudden changes occur in the intensity of the image.

4 Discussion

The present study demonstrates that careful interpretation of lightning VHF interferometer observations is required because the emission sources may have complex spatial and temporal properties while the resolution of a typical lightning interferometer is limited. Even for a simple case of two corona bursts with reasonable separation in space and time considered here, the simulation results show that entirely different views of the spatiotemporal evolution of the source can be obtained with different interferometer specifications and imaging parameters. On the positive side, this also means that great opportunities for advancing lightning physics await for lightning interferometry studies with improved resolution. It should be pointed out that in our simulation the bursts are at fixed locations and noise is not included for convenience, which will also make resolving the realistic corona bursts more challenging.

To resolve the corona bursts that occur in close space and time, the spatial resolution of the instrument is the key. When the main lobe of the instrument is too large, extending over an area larger than the spatial separation between the bursts, the max-

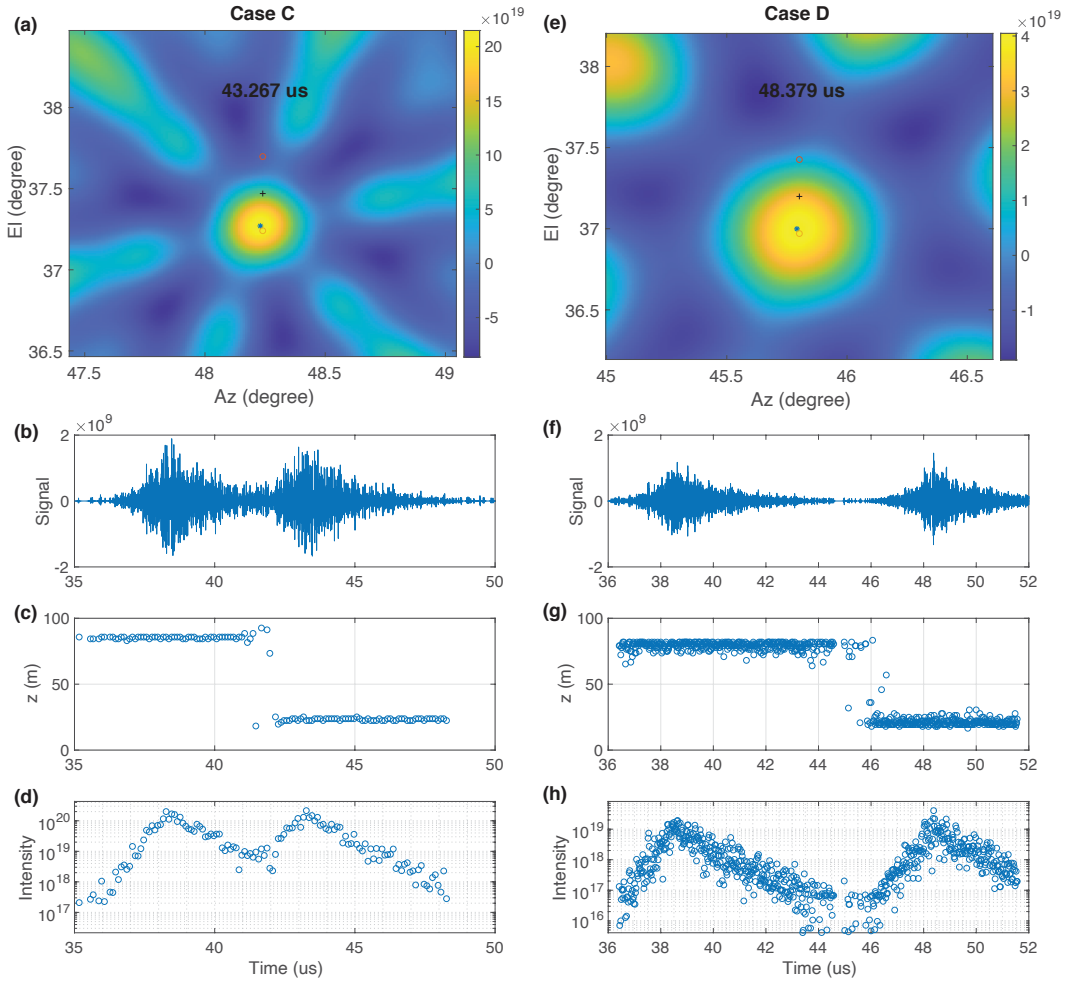

Figure 4. Results from simulation cases C and D. (a, e) The image with the highest intensity during the entire simulation. In the image, black '+' represents the center of the image, the two circles give the locations of the two streamer bursts, and '∗' shows the location of the maximum intensity pixel. (b, f) The bandwidth limited signal from the reference sensor. (c, g) The height of the maximum intensity pixel relative to 6 km altitude. (d, h) The value of the maximum intensity pixel.

imal intensity can appear at a location between them at the moment when the two bursts have comparable intensities. To improve the angular resolution λ/b, either the baseline, frequency, or both can be increased, as demonstrated by the simulation cases C and D. One factor that should also be taken into account is the source spectrum. The HF and VHF frequency spectrum of a corona burst is determined by the spectrum of individual streamers (Liu et al., 2019, 2020; Liu & Dwyer, 2020). Although the streamer spectrum considered here quickly rolls off above a few tens of MHz (see Figure S1), the recent study by Pu et al. (2021) indicates the streamer spectrum in lightning processes can extend to higher frequency range. Therefore, increasing the frequency of the sensor should be effective in improving the resolution for at least some lightning processes.

It is also worth implementing algorithms or methods that can improve the temporal resolution of the imaging, such as the beamforming technique. Increasing the temporal resolution helps through reducing the chance of streamers from any two bursts to occur within the time window of an image. Its effectiveness depends on the number of streamers in a corona burst and separation between the bursts. In addition, future studies should explore imaging techniques beyond time difference of arrival based approaches. Imaging algorithms utilizing larger numbers of baselines in Fourier based approaches combined with deconvolution such as CLEAN (Clark, 1980) are one direction similar to astronomical imaging. Multiple source direction of arrival algorithms based on covariance estimations such as MUSIC (Schmidt, 1986) are another direction. These algorithms have significant advantages for resolving ambiguities, using array degrees of freedom to enable estimation of multiple sources, and ultimately helping to resolve corona bursts. Additionally, these approaches are more suitable for the formal incorporation of array calibration to remove the effects of the interferometer element and array responses.

Finally, simulation can provide a good understanding of the dependence of the obtained source dynamics on the burst parameters to aid the analysis of the interferometer data. For instance, the apparent fast downward motion in Case A is inferred during the fall of the first burst and the rise of the second. The apparent speed then contains information about those times. In the case when radio sensors may be saturated during the corona bursts, and the interferometer does not have the resolution to resolve individual bursts, the apparent speed can still be determined (interferometry is generally robust in the case of signal saturation) and can still give information about the spatiotemporal evolution of the individual corona bursts. Another example is to understand and constrain the bidirectional development of fast breakdown reported by Huang et al. (2021). The bidirectional fast breakdown likely contains separate VHF sources that propagate either upward or downward. Simulations can provide the constraints on the source parameters in order for the sources to be resolved by a particular instrument. In fact, work is currently underway to simulate LOFAR observations to investigate accuracy and imaging artifacts of the LOFAR interferometry analysis (Scholten et al., 2021).

Open Research

The MATLAB scripts and functions used to obtain the results reported in the paper are available here: https://doi.org/10.5281/zenodo.5761824.

Acknowledgments

This research was supported in part by AFOSR Awards FA9550-18-1-0358 and FA9550-21-1-0366 to the University of New Hampshire and a subaward of DARPA HR00112120003 Grant to Embry-Riddle Aeronautical University.

References

Belz, J. W., Krehbiel, P. R., Remington, J., Stanley, M. A., Abbasi, R. U., LeVon,

R., ... Zundel, Z. (2020, December). Observations of the Origin of Downward Terrestrial Gamma-Ray Flashes. *J. Geophys. Res. Atmos.*, *125*(23), e31940. doi: 10.1029/2019JD031940

Clark, B. G. (1980, September). An efficient implementation of the algorithm 'CLEAN'. *Astron. Astrophys.*, *89*(3), 377.

Hare, B. M., Scholten, O., Dwyer, J., Ebert, U., Nijdam, S., Bonardi, A., ... Winchen, T. (2020, March). Radio emission reveals inner meter-scale structure of negative lightning leader steps. *Phys. Rev. Lett.*, *124*(10), 105101. doi: 10.1103/PhysRevLett.124.105101

Hare, B. M., Scholten, O., Dwyer, J., Trinh, T. N. G., Buitink, S., ter Veen, S., ... others (2019, Apr). Needle-like structures discovered on positively charged lightning branches. *Nature*, *568*, 360-363. doi: 10.1038/s41586-019-1086-6

Huang, A., Cummer, S. A., & Pu, Y. (2021, April). Lightning initiation from fast negative breakdown is led by positive polarity dominated streamers. *Geophys. Res. Lett.*, *48*(8), e91553. doi: 10.1029/2020GL091553

Liu, N. Y., & Dwyer, J. R. (2020, December). Thunderstorm high frequency radio bursts with weak low frequency radiation. *Geophys. Res. Lett.*, *47*(23), e90325. doi: 10.1029/2020GL090325

Liu, N. Y., Dwyer, J. R., & Tilles, J. N. (2020, July). Electromagnetic radiation spectrum of a composite system. *Phys. Rev. Lett.*, *125*(2), 025101. doi: 10.1103/PhysRevLett.125.025101

Liu, N. Y., Dwyer, J. R., Tilles, J. N., Stanley, M. A., Krehbiel, P. R., Rison, W., ... Wilson, J. G. (2019). Understanding the radio spectrum of narrow bipolar events. *J. Geophys. Res. Atmos.*, *124*, 10134-10153. doi: 10.1029/2019JD030439

Lyu, F., Cummer, S. A., Qin, Z., & Chen, M. (2019, Mar). Lightning initiation processes imaged with very high frequency broadband interferometry. *J. Geophys. Res. Atmos.*, *124*, 2994-3004. doi: 10.1029/2018JD029817

Marshall, T. C., Schulz, W., Karunarathna, N., Karunarathne, S., Stolzenburg, M., Vergeiner, C., & Warner, T. (2014, January). On the percentage of lightning flashes that begin with initial breakdown pulses. *J. Geophys. Res. Atmos.*, *119*, 445-460. doi: 10.1002/2013JD020854

Nag, A., DeCarlo, B. A., & Rakov, V. A. (2009, Feb). Analysis of microsecond- and submicrosecond-scale electric field pulses produced by cloud and ground lightning discharges. *Atmos. Res.*, *91*(2), 316-325. doi: 10.1016/j.atmosres.2008.01.014

Pu, Y., & Cummer, S. A. (2019, November). Needles and lightning leader dynamics imaged with 100-200 MHz broadband VHF interferometry. *Geophys. Res. Lett.*, *46*(22), 13,556-13,563. doi: 10.1029/2019GL085635

Pu, Y., Cummer, S. A., & Liu, N. (2021). VHF radio spectrum of a positive leader and implications for electric fields. *Geophysical Research Letters*, *48*(11), e2021GL093145.

Rison, W., Krehbiel, P. R., Stock, M. G., Edens, H. E., Shao, X.-M., Thomas, R. J., ... Zhang, Y. (2016). Observations of narrow bipolar events reveal how lightning is initiated in thunderstorms. *Nat. Commun.*, *7*. doi: 10.1038/ncomms10721

Schmidt, R. (1986). Multiple emitter location and signal parameter estimation. , *34*(3), 276–280.

Scholten, O., Hare, B. M., Dwyer, J., Liu, N., Sterpka, C., Buitink, S., ... Winchen, T. (2021a). Distinguishing features of high altitude negative leaders as observed with LOFAR. *Atmos. Res.*, *260*, 105688. Retrieved from `https://www.sciencedirect.com/science/article/pii/S0169809521002404` doi: https://doi.org/10.1016/j.atmosres.2021.105688

Scholten, O., Hare, B. M., Dwyer, J., Liu, N., Sterpka, C., Buitink, S., ... ter Veen, S. (2021b, September). Time resolved 3D interferometric imaging of a sec-

tion of a negative leader with LOFAR. *Phys. Rev. D*, *104*(6), 063022. doi: 10.1103/PhysRevD.104.063022

Scholten, O., Hare, B. M., Dwyer, J., Liu, N., Sterpka, C., Kolmasov, I., ... ter Veen, S. (2021, October). Interferometric imaging of intensely radiating negative leaders. *arXiv e-prints*, arXiv:2110.02547.

Shao, X.-M., Ho, C., Caffrey, M., Graham, P., Haynes, B., Bowers, G., ... Rassoul, H. (2018). Broadband RF interferometric mapping and polarization (BIMAP) observations of lightning discharges: Revealing new physics insights into breakdown processes. *J. Geophys. Res. Atmos.*, *123*(18), 10,326-10,340. Retrieved from `https://agupubs.onlinelibrary.wiley.com/doi/abs/10.1029/2018JD029096` doi: 10.1029/2018JD029096

Shi, F., Liu, N. Y., Dwyer, J. R., & Ihaddadene, K. (2019). VHF and UHF electromagnetic radiation produced by streamers in lightning. *Geophys. Res. Lett.*, *46*, 443-451. doi: 10.1029/2018GL080309

Shi, F., Liu, N. Y., & Rassoul, H. K. (2016). Properties of relatively long streamers initiated from an isolated hydrometeor. *J. Geophys. Res. Atmos.*, *121*, 7284–7295. doi: 10.1002/2015JD024580

Stock, M. (2014). *Broadband interferometry of lightning* (Doctoral dissertation, New Mexico Institute of Mining and Technology). Retrieved from `https://www.proquest.com/dissertations-theses/broadband-interferometry-lightning/docview/1660201463/se-2`

Stock, M. G., Akita, M., Krehbiel, P. R., Rison, W., Edens, H. E., Kawasaki, Z., & Stanley, M. A. (2014). Continuous broadband digital interferometry of lightning using a generalized cross-correlation algorithm. *J.Geophys. Res. Atmos.*, *119*, 3134–3165. Retrieved from `http://dx.doi.org/10.1002/2013JD020217` doi: 10.1002/2013JD020217

Stock, M. G., Krehbiel, P. R., Lapierre, J., Wu, T., Stanley, M. A., & Edens, H. E. (2017). Fast positive breakdown in lightning. *J. Geophys. Res. Atmos.*, *122*, 8135-8152. Retrieved from `https://agupubs.onlinelibrary.wiley.com/doi/abs/10.1002/2016JD025909` doi: 10.1002/2016JD025909

Sun, Z., Qie, X., Liu, M., Cao, D., & Wang, D. (2013, July). Lightning VHF radiation location system based on short-baseline TDOA technique — Validation in rocket-triggered lightning. *Atmos. Res.*, *129*, 58-66. doi: 10.1016/j.atmosres.2012.11.010

Tilles, J. N. (2020). *Broadband radio mapping and imaging of lightning processes* (Doctoral dissertation, University of New Hampshire, Durham, NH). Retrieved from `https://scholars.unh.edu/dissertation/2519`

Tilles, J. N., Krehbiel, P. R., Stanley, M. A., Rison, W., Liu, N. Y., Lyu, F., ... Wilson, J. (2020, October). Radio interferometer observations of an energetic in-cloud pulse reveal large currents generated by relativistic discharges. *J. Geophys. Res. Atmos.*, *125*(20), e32603. doi: 10.1029/2020JD032603

Tilles, J. N., Liu, N. Y., Stanley, M. A., Krehbiel, P. R., Rison, W., Stock, M. G., ... Wilson, J. G. (2019). Fast negative breakdown in thunderstorms. *Nat. Commun.*, *10*. doi: 10.1038/s41467-019-09621-z